

Fiber-fed Pulsed Plasma Thruster (FPPT) for Small Satellites

IEPC 2019-A899

Presented at the 36th International Electric Propulsion Conference

University of Vienna • Vienna, Austria

September 15-20, 2019

Curtis A. Woodruff¹, Darren M. King², Rodney L. Burton³, and David L. Carroll⁴
CU Aerospace (CUA), Champaign, IL 61822

Abstract: The extensive flight legacy of the Pulsed Plasma Thruster (PPT) has been limited to attitude control and station keeping missions by low thruster efficiency, high specific mass, and for some missions, low specific impulse. The coaxial Fiber-fed Pulsed Plasma Thruster (FPPT) for small satellites can enable high impulse primary propulsion missions by the combination of a user-controlled Teflon fiber feed system employing a different propellant $j \times B$ topology from that of classic PPT configurations, a regenerative carbon igniter, and low mass ceramic capacitors. A major enhancement of the FPPT technology is the ability to control the propellant feed rate along with the pulse energy, thereby providing control of both specific impulse and thrust. The FPPT flight design and performance results are presented, and a simplified model of plasma acceleration is discussed.

Nomenclature

B	= magnetic field normal to current, Tesla	PTFE	= polytetrafluoroethylene (C_2F_4) _n [Teflon]
b	= constant in thrust equation, non-dimensional	r_a	= anode radius, m
dt	= differential time step, s	r_c	= cathode radius, m
E	= electric field, V/m	r_I	= radius of region I, m
e	= electron or ion charge, 1.6×10^{-19} coulombs	r_{II}	= radius of region II, m
g	= gravitational acceleration, 9.81 m/s^2	s/c	= spacecraft
I	= pulse current, amperes	T	= thrust, N
I_{sp}	= specific impulse U_e/g , seconds	U_c	= Alfvén critical speed, km/s
J	= energy, joules	U_e	= propellant exhaust velocity = gI_{sp} , m/s
j	= current density, amperes/m ²	ΔV	= $g I_{sp} \ln(m_o/m_f)$, m/s
$j \times B$	= electromagnetic force density, N/m ³	α	= degree of ionization
L'	= inductance gradient, H/m	η_{PPU}	= PPU efficiency, power output / input
m	= ablated propellant mass per pulse, kg	μ_o	= vacuum permeability, $4\pi \times 10^{-7} \text{ H/m}$
m_e	= mass of electron, kg	Ω	= electron Hall parameter, $\omega_B/v_c = eB/m_e v_c$
PPU	= Power Processing Unit	Ω^+	= ion Hall parameter for neutral collisions
PPT	= Pulsed Plasma Thruster	Ψ	= action integral $\int f^2 dt$, A ² -s

I. Introduction

The pulsed plasma thruster (PPT) [Burton, 1998] has long been an attractive technology for satellite propulsion. The PPT uses solid propellant and therefore inherently eliminates the possibility of propellant leakage and undesirable leakage thrust. The first electromagnetic PPT flight was on the Soviet Zond II Mars mission in 1964

¹ Senior Engineer, woodruff@cuaerospace.com.

² Laboratory Director, king@cuaerospace.com.

³ VP for Research, burton@cuaerospace.com.

⁴ President, carroll@cuaerospace.com.

[Burton, 1998]. One of the first published papers on the PPT was in 1965 [Guman, 1965]. After Zond II, important PPT flights occurred in 1981 (TIP/Nova) [Ebert, 1989; Hoffman, 1992], 1968 (LES-6) [Guman, 1970] and 2000 (EO-1) [Benson, 2000; Zakrzewski, 2002]. Despite this extensive flight history, fundamental improvements still remain to be made in PPT propulsion systems, and we present several such advances in this paper.

The classic PPT is shown in **Fig. 1**. Energy is derived from a capacitor charged by a PPU source, Teflon propellant is spring-loaded against a stop (located on the anode in **Fig. 1**), a spark plug igniter is located in the cathode, and the electrodes are parallel plates or coaxial. **Figure 1** also shows the direction of the current j and self-induced magnetic field B , resulting in an accelerating electromagnetic force $j \times B$. Note that this topology creates a magnetic field in the PTFE, so that sublimating propellant is ionized in a strong B field. Also note that the ablated mass m for each pulse is not independently controlled, but is determined only by the geometry and the pulse energy, and as mass is consumed the spring advances the propellant against the stop.

In reality the picture is more complicated than shown in **Fig. 1**. Initial current breakdown occurs near the igniter (spark plug) at the propellant face, and the current does not flow completely normal to the electrodes as shown, but is tilted. The pulse circuit can oscillate, reversing the current direction, and the reversed second half cycle then initiates at the propellant face, not downstream, leaving a complex distribution of current density j and magnetic field B between the electrodes. Not all the Teflon is ionized, contributing a fraction of electrothermal thrust and reducing specific impulse. Finally, development of a reliable spark igniter with a life of $\sim 10^8$ pulses has proven to be a challenge.

The classic parallel plate PPT has additional drawbacks for the propulsion of small satellites. The tilting current creates an off-axis electromagnetic thrust component, although this can be overcome by firing pairs of back-to-back thrusters, as was done with LES-8/9 [Vondra, 1974] or by using a coaxial geometry with multiple igniters. In addition, the parallel plate electrode geometry creates large pulsed fringing B fields, with the potential of inducing currents in the satellite bus, a problem that can be overcome with a coaxial geometry.

Because of the drawbacks with parallel plate geometries, coaxial geometries are attractive. After pursuing a number of designs, the coaxial PPT-11 thruster (**Fig. 2**) was thoroughly investigated [Laystrom, 2003; Burton, 2009; Burton, 2011a; Burton, 2011b]. The Teflon propellant was spring-fed, with four curved PTFE bars side-fed to a central anode. The 30 kA discharge pulse was initiated by a Unison Industries semiconductor igniter and generated by a Unison 70 J mica capacitor bank [Benson, 2001].

Peak performance of the PPT-11 was 1375 seconds I_{sp} at 13.7% efficiency with a pulse energy of 70 J [Laystrom, 2003]. A major limitation was the relatively small total propellant mass as limited by the geometry. Thus, despite the attractive performance, and an improved specific mass of 50 g/W, the PPT-11 design is not satisfactory for use in high impulse missions.

Although all PPT flight propulsion to date has been limited to ACS or station keeping for small satellites, larger satellite propulsion was also investigated with the development of the One Millipound Thruster (OMT) with a specific impulse of 1600 s at 4.4 mN [Palumbo, 1979]. With a maximum stored energy of 750 J and 11.3 kg of Teflon propellant, the OMT thruster wet mass was 45 kg [Vondra, 1980]. The OMT used a side-fed parallel plate geometry

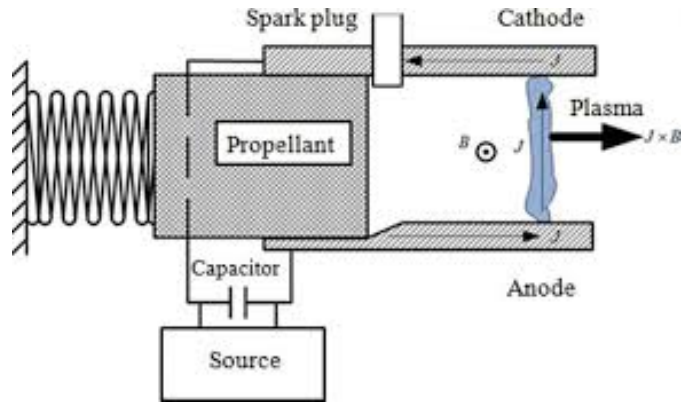


Figure 1. Schematic of classic parallel plate PPT [Huang, 2015].

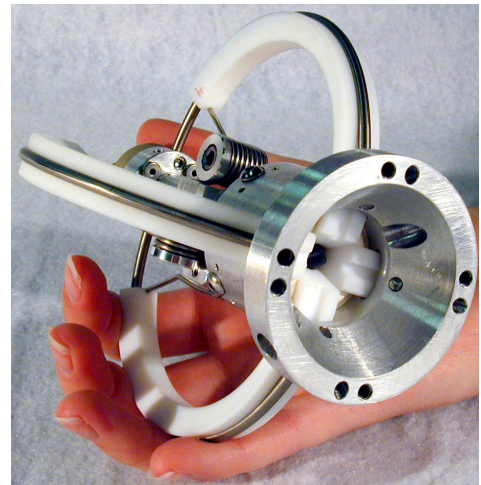


Figure 2. CUA PPT-11 coaxial pulsed plasma thruster [Laystrom, 2003] with $I_{sp} \sim 1200$ s and specific thruster dry mass = 50 g/W. PPT-11 is shown with central anode, outer cathode, and four curved propellant bars.

with cylindrical envelope dimensions of 61 cm diameter by 30 cm high (89 liters) and was envisioned for use on satellites up to 500 kg. The typical pulse rate was 0.2 Hz, with a max power consumption of 170 W, resulting in a specific mass of 200 kg/kW, a technology far too large and massive for small satellites.

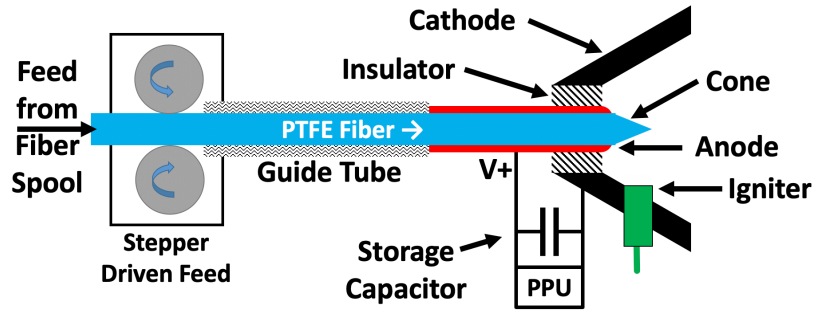


Figure 3. Cross-section schematic of the Fiber-fed Pulsed Plasma Thruster (FPPT) [Woodruff, 2019a].

II. Fiber-fed Pulsed Plasma Thruster (FPPT) Design

Acceptable parameters for adapting the PPT to small satellites imply an order of magnitude reduction in thruster specific mass and volume. This has been accomplished with the fiber-fed pulsed plasma thruster (FPPT), Figs. 3 and 4 [Woodruff, 2019a; Woodruff, 2019b].

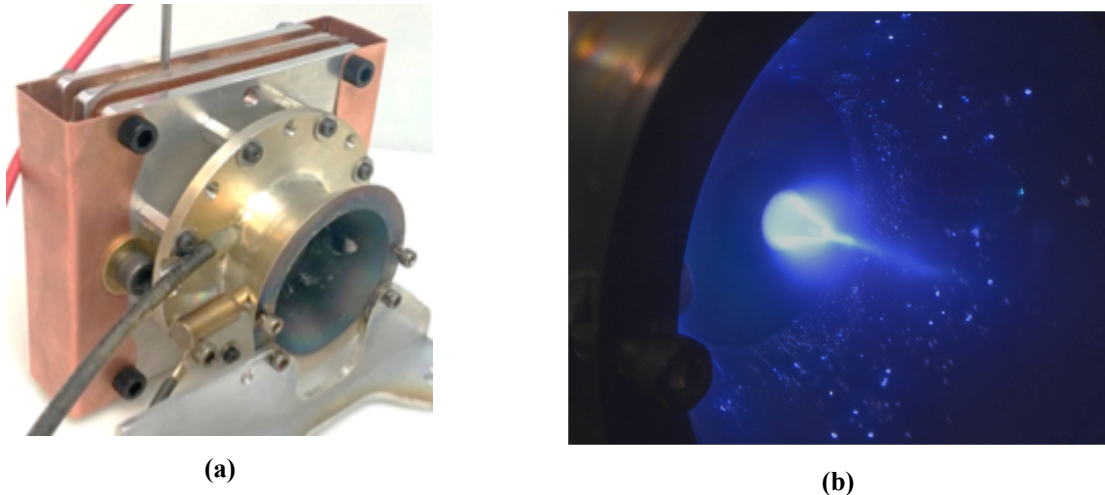


Figure 4. Photographs of the Fiber-fed Pulsed Plasma Thruster (FPPT) with 16 J capacitor bank (a) and during operation (b) [Woodruff, 2019a]. The discharge displays a central pinch column and cathode spots.

The following improvements were implemented in the FPPT system to address the aforementioned PPT issues:

1. The FPPT uses coaxial geometry, with a central anode, on-axis propellant feed, and multiple igniters (sequentially-fired) located in the outer cathode.
2. The propellant is stored in the form of 3.2 mm diameter PTFE (Teflon) fiber. The flexibility of this fiber simplifies the feed system and enables compact propellant storage and packaging.
3. Energy is stored in 1000 V (rated) ceramic capacitors, each with a unit volume of $\sim 0.1 \text{ cm}^3$ and unit stored energy of 25 mJ. This low volume multi-layer ceramic capacitors (MLCC) approach avoids possible leakage from oil-filled capacitors and creates packaging flexibility.
4. A robust coaxial regenerative carbon igniter (RCI) [Woodruff, 2019c] captures discharge carbon plated onto the igniter insulator and electrodes. Multiple RCIs are fired serially to fire the FPPT.

5. The topology of the current and propellant is different from that of the classic parallel plate configuration in that the propellant is fed along the axis, and its sublimation surface experiences zero B-field and high $\mathbf{j} \times \mathbf{B}$ pinch pressure. The classic PPT plasma acceleration physics are correspondingly modified.

III. Electrode Geometry

The electromagnetic contribution to thrust is predicted for coaxial geometries by:

$$T = (\mu_0/4\pi) I^2 [\ln(r_c/r_a) + b] \quad (1)$$

where $1/4 < b < 3/4$ [Jahn, 1968]. For current pulses, the integration over the current pulse of the thrust equation, assuming that the discharge geometry is invariant, results in an impulse bit proportional to the action integral $\Psi = \int I^2 dt$. Comparison of the predicted impulse bit to the total impulse bit measured on the thrust stand shows that the FPPT electromagnetic contribution to thrust is 70-90%, with the percentage increasing with discharge energy.

As with any coaxial electromagnetic thruster, it is tempting to increase the radius ratio of the outer electrode to the inner electrode, so as to increase $\ln(r_c/r_a)$ and take advantage of the higher thrust and dynamic impedance $L'U_c/4$. From work with quasisteady magnetoplasma-dynamic thrusters [Ek Dahl, 1967; Burton, 1983] it is known that for sufficiently large r_c/r_a the discharge can collapse from azimuthal symmetry into a radial spoke. While it is not known what the r_c/r_a limit is for pulsed (not quasi-steady) PPTs, the FPPT presently uses $r_c/r_a \approx 6$ with no evidence of spoking. The electrode geometry is shown in **Fig. 3**.

IV. FPPT Performance

A flight design of the FPPT (**Fig. 13** of [Woodruff, 2019a]) has a volume of 1 liter including propellant and a thruster dry mass of ~1200 g, achieving an order-of-magnitude improvement in specific mass and volume impulse. The performance envelope of 1U flight and 1.5U versions of the FPPT is summarized in **Table 1** for different bank energies, power levels and measured values of specific impulse. Note that the 1.5U version has a larger capacitor bank that enables higher energy and consequently higher I_{sp} pulses.

Table 1. FPPT Flight Unit performance for various modes of operation.

Item	FPPT Performance			
Propellant	PTFE Teflon			
FPPT system specific mass	20 g/W @ peak power			
Functional temperature range	-10 to +60 °C (expected)			
FPPT System volume	1.0 Liter	1.5 Liters		
Propellant storage volume	0.15 Liters	0.40 Liters		
Initial propellant mass	0.33 kg	0.87 kg		
Total FPPT dry mass	1.5 kg	2.8 kg		
Capacitor bank energy	16 J	32 J		
Bus input power ($\eta_{PPU} = 85\%$)	48 W	48 W		
Thruster pulse rate	2.6 Hz	2.6 Hz	1.3 Hz	1.3 Hz
FPPT Thrust (thrust stand)	0.33 mN	0.28 mN	0.35 mN	0.27 mN
Specific Impulse	1,000 s	1,700 s	1,600 s	2,400 s
Total Impulse	3,260 N-s	5,640 N-s	13,500 N-s	20,700 N-s
Volumetric Impulse	3,260 N-s/L	5,640 N-s/L	9,000 N-s/L	13,800 N-s/L
Spacecraft ΔV , 5 kg wet s/c	670 m/s	1,140 m/s	3,000 m/s	4,500 m/s
Spacecraft ΔV , 14 kg wet s/c	235 m/s	395 m/s	1,000 m/s	1,510 m/s

V. Propellant Ablation

One of the key FPPT innovations is independent control of the mass flow rate of PTFE fiber and the energy per pulse. As shown in **Fig. 5**, higher fiber feed rate results in a longer cone, with higher exposed surface area. Because of the $j \times B$ pinch forces, the surface is uniformly exposed to the discharge, resulting in an ablated mass approximately proportional to surface area. For a given discharge energy, higher ablated mass results in lower plasma enthalpy (J/kg) and lower specific impulse. To maintain constant cone height, the feed rate must be increased in proportion to the discharge energy, as would be expected.

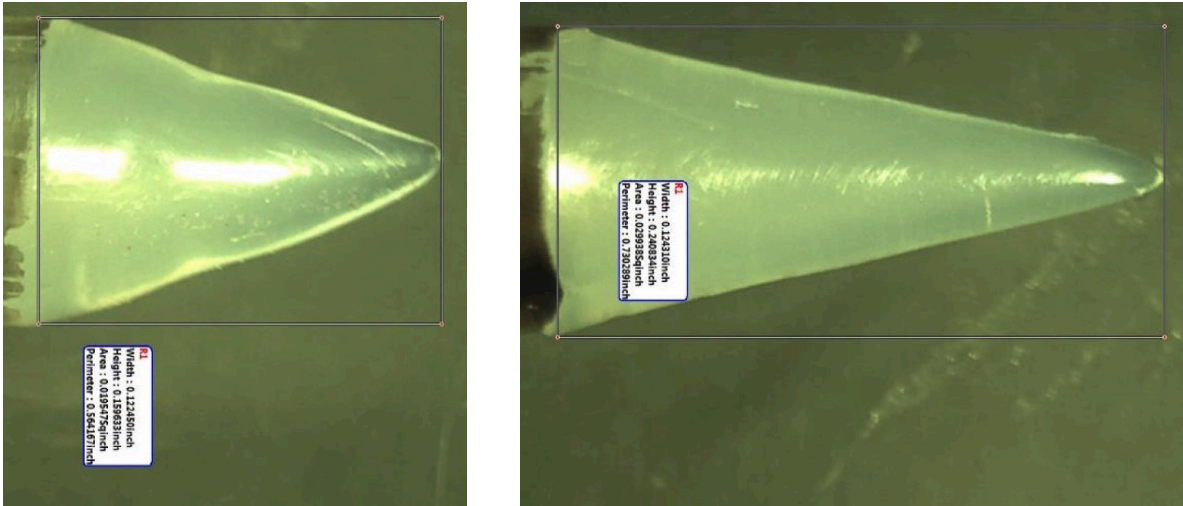


Figure 5. Steady-state conical PTFE tip at low feed rate and high I_{sp} (left) and higher feed rate and lower I_{sp} (right).

Figure 6 shows the result of a test at 32 J, starting with a long cone and maintaining zero feed rate. The cone is observed to ablate to a much shorter height over 10,000 pulses.

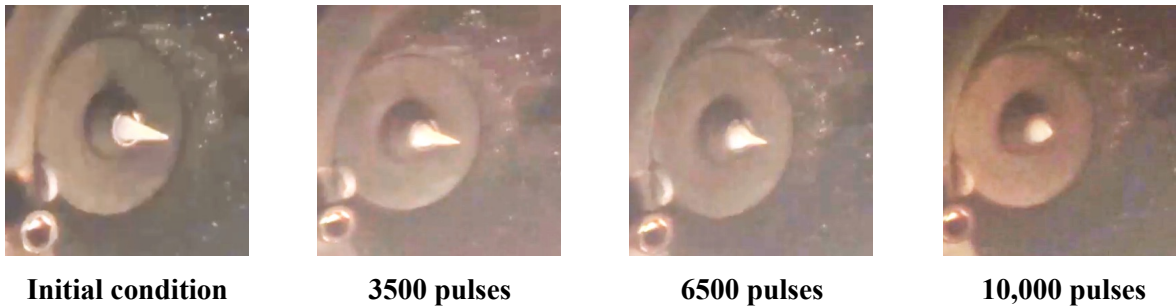


Figure 6. Zero feed rate evolution of FPPT cone shape over 10,000 pulses at 32 J and 2.8 Hz.

VI. Electrode Erosion

The small size of the anode in the coaxial FPPT geometry, and the requirement of $>10^8$ pulses for high total impulse, requires that close attention be paid to anode erosion. The unique electrode/propellant topology of the FPPT creates a situation in which anode erosion can be virtually eliminated by operating in a carbon-regenerative mode, as has been indicated during testing.

The FPPT central anode is annular, with a total current attachment area measured in mm^2 , compared to the parallel plate PPT, with an anode area of many cm^2 . Peak anode current density is $j \sim 1 \times 10^9 \text{ A/m}^2$. Because the radial $\mathbf{j} \times \mathbf{B}$ pinch effect creates a magnetic pressure that varies as $(I/r)^2$, the stagnated gasdynamic pressure at zero magnetic field is highest at the tip of the cone (minimum radius) and reduces toward the base of the cone (larger radius). The conical propellant tip, operating in a region of zero magnetic field, thus provides a pressure gradient that forces sublimated and dissociated carbon (and fluorine) atoms backwards toward the anode, as shown in **Fig. 7**, where carbon atoms can plate out. The result in essence is a carbon anode that regenerates with each pulse, effectively eliminating metallic erosion. **Figure 7** shows Regions I and II, which are described in more detail in **Section VIII**.

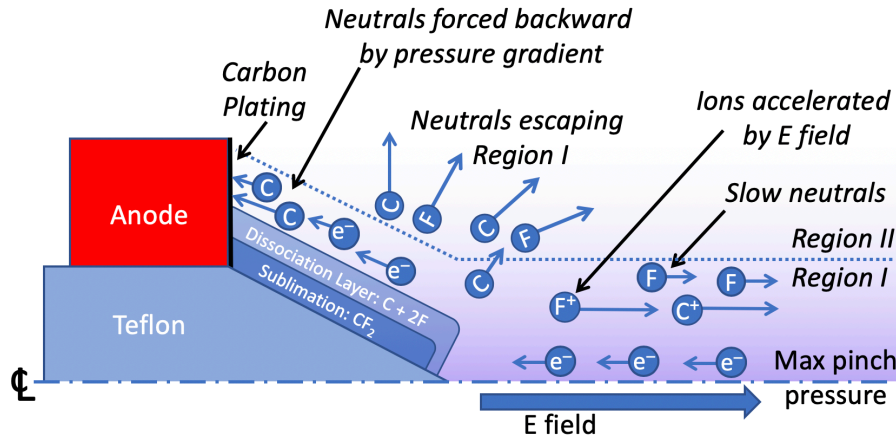


Figure 7. The high-pressure gradient (plasma pinch) Region I drives carbon (C) atoms onto the anode. Ions (C^+ and F^+) accelerate in the direction of the pinched E -field, as neutrals escape into Region II.

The surface area of the cathode is measured in cm^2 , so that cathode erosion is inherently less significant than anode erosion. As was observed with PPT-11 [Laystrom, 2003], carbon also plates onto the cathode (and onto the igniters). This regenerative carbon process implies that electrode (and igniter) erosion is a manageable wear issue with the FPPT.

A similar regenerative carbon effect occurs with the coaxial regenerative carbon igniters (RCI) spark igniters (**Fig. 8**) being developed for the FPPT [Woodruff, 2019a]. The RCIs rely on a high resistance carbon layer that is located on the insulator surface and is regenerated by carbon plating during thruster operation.

The FPPT uses a redundant array of four radial igniters in the cathode, fired sequentially. Igniter operation and discharge ignition have operated normally throughout the test program, and two igniters have demonstrated > 1 million pulses collectively with erosion $< 40 \text{ ng/pulse}$ consistent with a life of $> 1 \times 10^8$ pulses.



Figure 8. Photograph of CUA regenerative carbon igniter (RCI) [Woodruff, 2019a].

VII. Plasma Acceleration and Thrust

The Fiber-Fed Pulsed Plasma Thruster (FPPT), **Fig. 4**, operates in a distinctly different mode from the classic rectangular or coaxial PPT modes, **Fig. 9**. Classic electromagnetic accelerators can operate in two modes: one with a stationary current at the propellant surface called deflagration mode [Burton, 1969; Cheng, 1971], or one with a moving, "snowplow" current sheet called detonation mode [Burkhardt, 1962; Burton, 1968; Polzin, 2019]. The FPPT operates in what could be called an anchored deflagration mode, in that the discharge current is constrained along the sublimating PTFE surface, a constraint that does not occur in the classic PPT.

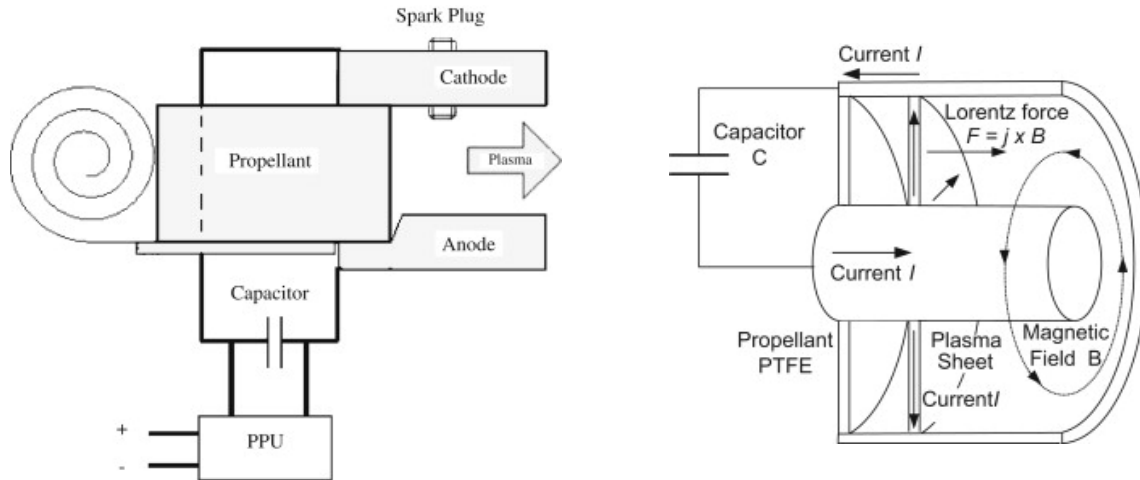


Figure 9. Classic PPT in rectangular [Dali, 2008] and coaxial [Krejci, 2013] geometries. The PTFE propellant surface experiences high magnetic field between cathode and anode. The discharge is initiated in a plasma sheet along the propellant face. The direction of the Lorentz force $j \times B$ is pointed away from the propellant surface in both geometries.

The FPPT is a coaxial device with propellant feed on the centerline through the anode, **Fig. 3**. The PTFE propellant surface experiences zero magnetic field. The flexible PTFE propellant fiber is fed at a commanded rate, which can be varied with the discharge energy and pulse rate, ablating into a constant geometry conical shape at the tip. The initial voltage breakdown in PPT thrusters occurs when igniter-produced electrons accelerate to the anode and insulator regions, creating sputtered ions followed by a fast current pulse, **Fig. 10**.

For the classic PPT, the electrode geometry creates an E -field perpendicular to the thrust direction, with current parallel to E , **Fig. 11a**. The self-induced $j \times B$ force is perpendicular to the propellant face, directed *away* from the surface. In the FPPT, the self-induced $j \times B$ force is also normal to the propellant face, but is directed *toward* the surface in the immediate vicinity of the propellant, **Fig. 11b**.

The field topology of the FPPT is reversed and occurs because the PTFE fiber is fed on-axis, creating a zero B -field condition in the fiber. The high discharge current (10s of kA) produces a $B_\theta[r, z]$ magnetic field as high as 2 Tesla. The strong self-pinch $j \times B$ region on axis and on the fiber creates an on-axis pressure as high as 1.6 MPa. The conical geometry produces a $j \times B$ force component in the negative z direction, anchoring the current to the PTFE cone. While deflagration mode operation is suspected based on the sublimating mass source, deflagration has not yet been experimentally verified.

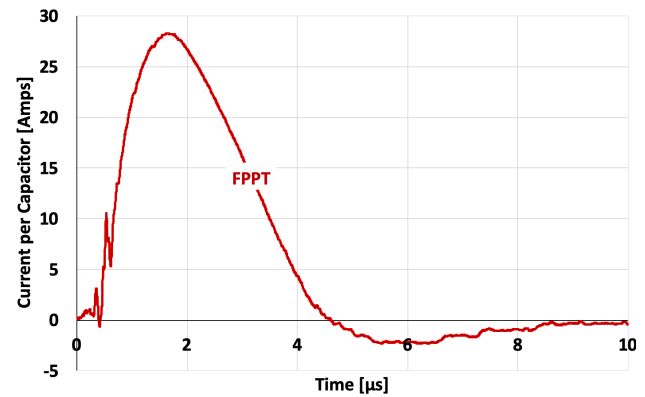


Figure 10. Measured per-cap current waveform for the FPPT current pulse.

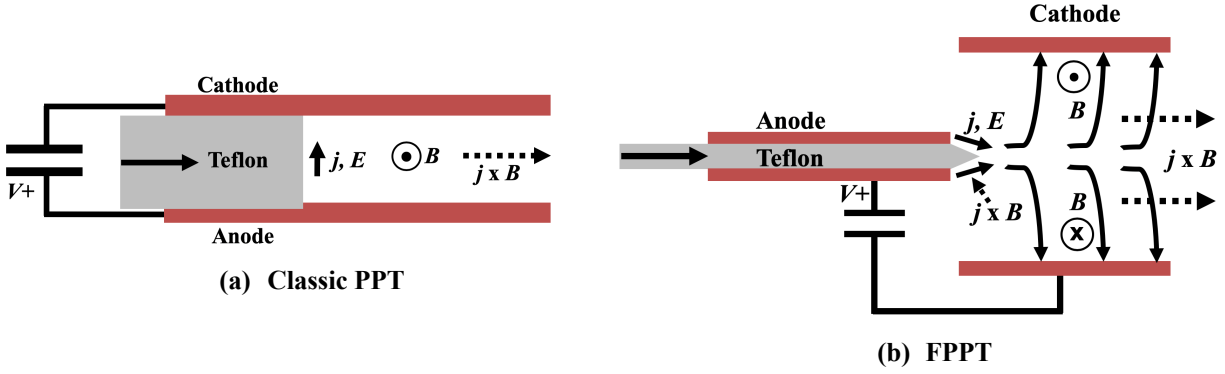


Figure 11. Geometry and field lines for (a) Classic PPT, and (b) FPPT. The direction of the Lorentz force $j \times B$ is away from the propellant surface in the classic geometry, but is directed towards the surface in the FPPT, creating a high pressure plasma pinch.

Detailed magnetic/electric probe measurements of the FPPT discharge volume have yet to be performed. Lacking these, the discharge is believed to be azimuthally symmetric in deflagration mode, based solely on photographic plus electrode and propellant erosion evidence. The FPPT can be characterized in terms of two distinct regions: a high density pinch region along the axis dominated by scalar ion and electron current, and a lower density region filling the remainder of the interelectrode volume, dominated by Hall current. The coaxial geometry forces the electric field to be axial near the centerline, as shown, producing axial current in that region. Since the thruster exit pressure falls to zero, a strong pressure gradient exists along the axis that accelerates ions and neutrals.

VIII. Simplified Model

A simplified descriptive model is used to describe essential features of the plasma conditions in the FPPT discharge, using thrust stand measurements for calibration. The plasma is initially created by radiative sublimation [Antonsen, 2005] of PTFE propellant at the anode tip from the several- μ s megawatt-level current pulse. Sublimated molecular species are dissociated into a swarm of C and F atoms from the $(CF_2)_n$ polymer. It is estimated, based on arcjet calculations at kW power levels [Megli, 1996], that the plasma is two-temperature, with a heavy particle temperature of 2 – 3 eV, and an electron temperature 4 – 9 eV. Many of the atoms are quickly ionized, generating a neutral plasma of carbon and fluorine neutrals and ions. The remaining thermal neutrals then expand radially away from the anode tip at a velocity of 2 - 4 cm/ μ s. While experimental results with PTFE show that double and triple ions exist, their exhaust velocity increases with ionization level. The simplified model assumes only single ions with a mass equivalent to the average mass of C + 2F, consistent with the assumption of a single exhaust velocity for all charged particles. The model assumes a flat-top unipolar current pulse with amplitude and pulse length values selected to agree with measured stored capacitor charge CV_0 , and measured action integral $\int I^2 dt$ for 16 J at 1700 s I_{sp} . The simplified model ignores effects due to late time ablation [Antonsen, 2005] and assumes that the post-pulse ablated mass is zero. A uniform thruster exit velocity of all ions at velocity gI_{sp} is also assumed.

The discharge volume (**Fig. 12**) is modeled with two regions: a high-density region I along the axis, of radius r_I , and an outer region II, of outer radius $r_{II} = r_c$. The high plasma density makes the electron Hall parameter $\Omega \ll 1$ in region I. The region I electrical conductivity σ is scalar and independent of radius [Cohen, 1973], an assumption that is nearly the same as a constant electron temperature approximation. The radius r_I of region I is assumed constant, with constant axial current density j_z . Region II, from radius r_I to radius r_c , is populated at a much lower density by neutrals ejected from region I. The model assumes that the region II current density is radial, and that the magnetic field is $B_\theta(r, z)$. The current and B_θ field then produce axial $j_z B_\theta$ thrust.

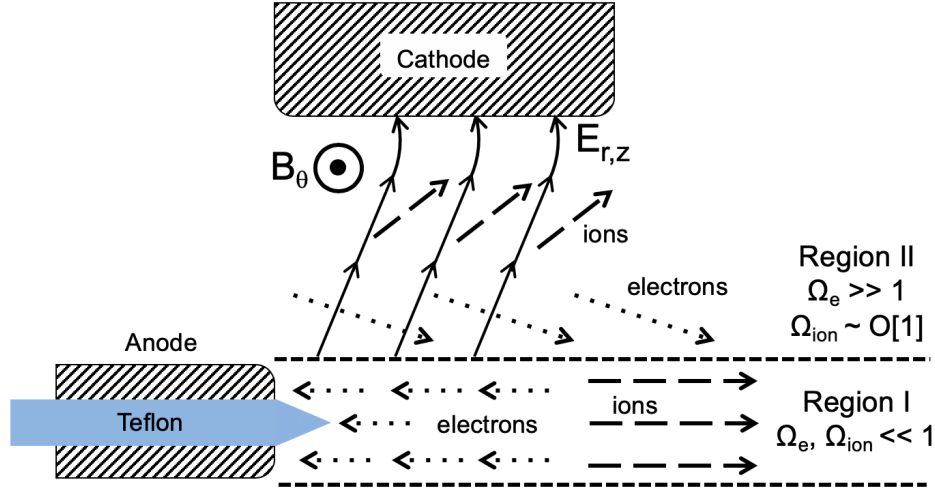


Figure 12. Simplified model of current conduction and particle motion in regions I and II.

Model: contributions to thrust

The plasma acceleration process begins at the anode tip region. Ions accelerated by eE_z are slowed by ion-neutral elastic collisional drag and charge exchange collisions. Elastic collisions of an accelerated ion with a thermal neutral can have two results: the ion can lose its momentum, effectively heating the neutral, or the ion can undergo a charge exchange collision with the slower neutrals, creating fast axial neutrals and slow ions, which are subsequently accelerated by eE_z . The net result of both types of ion-neutral collisions is a drag effect on the population of accelerated ions. Axial pressure decreases to zero at the thruster exit plane, a pressure gradient that primarily accelerates neutrals. The ion velocity is "supersonic" (higher than the thermal velocity), and the pressure acceleration of the ions is therefore small in comparison to eE_z .

The FPPT thrust is predominantly $\mathbf{j} \times \mathbf{B}$ with a 10-30% electrothermal contribution. For region I the $\mathbf{j} \times \mathbf{B}$ force is:

$$T_I = (\mu_0/4\pi) I^2 [\ln(r_I / r_a) + 0.50] \quad (2)$$

where the constant $b = 0.50$ results from the radial $\mathbf{j} \times \mathbf{B}$ force that generates a pressure on the anode tip [Jahn, 1968]. In region II the $\mathbf{j} \times \mathbf{B}$ thrust is:

$$T_{II} = (\mu_0/4\pi) I^2 \ln(r_c / r_I) \quad (3)$$

Model: contributions to current conduction

Region I. Current conduction in region I is relatively uncomplicated. The E_z field and scalar σ create an axial electron drift velocity. E_z and some ∇p also accelerate the ions, which are constrained along the axis by the radially inward $eV_z B_\theta$ Lorentz force. Ion slip velocity relative to neutrals is restrained to the Alfvén Critical Speed $U_c = 13.2$ km/s [Burton, 2000] by neutral ionization processes. The ions are slowed by neutral elastic collisions, thermalizing neutrals and scattering them out of region I. The ions are also slowed by charge-exchange collisions with neutrals, creating fast streaming neutrals and slow ions, reducing the mean ion velocity. The ion-neutral drag effect will be strongest near the anode tip, and will weaken as neutrals are ionized and thermally expand out of region I. The axial ion acceleration increases with distance as the heavy particle density and drag decrease.

The region I electron drift velocity occurs in an accelerating ion-neutral reference frame. This has the effect, as distance increases from the anode, of increasing the ion current and decreasing the electron current. The E_z field eventually falls to zero, as does B_θ , at the thruster exit. The region I Hall parameter is $\Omega \ll 1$, and the electron conductivity for the Teflon plasma is estimated as 16,000 S/m, for $T_i = 30,000$ K and $T_e / T_i = 3$ (Fig. 13).

Region II. The current conduction process in region II is considerably more difficult to resolve. Photographs show electron-emitting cathode spots (**Fig. 4**), which can form in ~ 10 ns [Schwirzke, 1993]. Early in the pulse, region I neutrals and cathode spot electrons populate region II. The electric field is primarily radial, and initial current is predominantly carried by electrons. These electrons then execute $E \times B$ drift toward the axis and the exit plane while ionizing region II neutrals (**Fig. 12**). The resulting ions drift toward the cathode and exit plane while colliding with neutrals from region I.

The net electron and ion currents are predominantly radial, producing $j_r B_\theta$ thrust. If it is assumed that the E and B fields vary as $1/r$, and also have the same dependence in z , then the electron and ion E/B drift velocities are constant in region II. The model postulates that both the E/B drift velocity and the region I exit ion velocity are equal to the exit velocity gI_{sp} as measured on the thrust stand. The ion Larmor radius $R^+ = m^+ V^+ / e B_\theta$ is typically a few mm, smaller than the interelectrode spacing, permitting ion gyration. The electron Larmor radius is μm in size.

The model uses region I conditions to estimate region II conditions. Employing the total voltage drop and conductivity σ , the dimensions of the cylindrical region I are typically 12 mm in length with a 4 mm radius. This permits calculation of the thrust contribution from region I, and from that the density of the exiting ion beam. Given the known thrusts from **Eqs. 2 and 3**, the region II ion density can be calculated.

The major remaining unknown is the region II degree of ionization α_{II} , which must be determined in order to calculate the collision frequency for ion-neutral collisions and the ion Hall parameter. From comparison of thrust stand measurements with **Eq. 1**, the thrust contribution from the neutrals is 10 – 30% of the total. Because the neutrals exit at a low velocity (3-6 km/s), the neutral density is $n_n \sim 0.8n^+$. The result is an ion Hall parameter $\Omega^+ \sim O[1]$. Ions will therefore drift at an angle to the E -field, as indicated in **Fig. 12**.

Model: contributions to discharge voltage

In region II, the thrust is primarily generated by $j \times B$ (**Eq. 3**). The resulting power is IV_{II} and, absent ohmic heating, equals the thrust power $\frac{1}{2} T U_e$. With U_e specified, the thrust is proportional to V_{II} . Ignoring neutral thrust and inductive voltage drop in region II:

$$V_{II} = (\mu_0 I / 2\pi) \ln(r_c / r_i) U_e \quad (4)$$

The ion acceleration voltage V_I in region I is similarly proportional to T_I :

$$V_I = (\mu_0 I / 2\pi) [\ln(r_i / r_a) + b] U_e \quad (5)$$

Considering remaining voltage drops, the voltage drop from electron conductivity σ was discussed above. An additional voltage loss is created by ion-neutral collisions, which increases with ion velocity and thermalizes the neutrals. The remaining voltage drops are the cathode and anode sheath voltages, which scale with ionization potential and are tens of volts. The total of all voltage drops is then compared to the measured discharge voltage to validate the model.

A model prediction of discharge impedance is shown in **Table 2**, for several contributing factors. The largest contributor, approximately 40% of the total, is predicted to be electron ohmic resistance in region I.

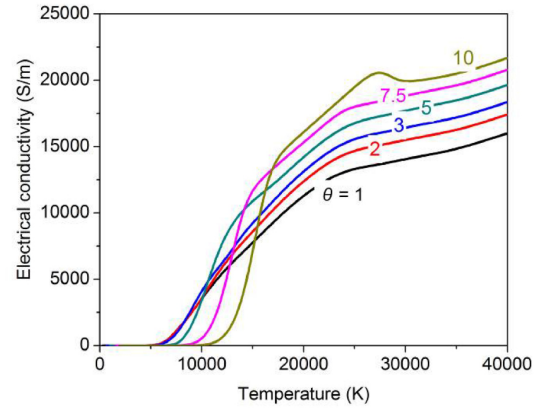


Figure 13. Electrical conductivity of PTFE plasma [Wang, 2017].

Table 2. Components of FPPT discharge impedance.

Component of impedance	Model Impedance (m Ω)	%
Sublimation, dissociation and ionization of PTFE	1.1	4
Region I electron ohmic resistance	12.4	40
Region I ion E_z field acceleration	4.7	15
Region I EM impedance from $j\mathbf{x}\mathbf{B}$ acceleration	1.9	6
Region II EM impedance from $j\mathbf{x}\mathbf{B}$ acceleration	5.3	17
Impedance of cathode and anode sheaths	5.7	18
Total discharge impedance	31.1	100

IX. Concluding Remarks

Because the FPPT exhausts neutral plasma, a neutralizer is not required. Nor are magnets required, as the B_0 field is self-induced. The system specific mass is low, and the specific impulse is variable. Total impulse is high, enabling high ΔV . These features make the FPPT attractive for small satellites.

A simplified descriptive model is introduced and was tuned with thrust stand measurements. Region I appears to bear similarities to a classic self-field MPD thruster if operated with reversed polarity. Because the FPPT central electrode is a tubular anode with the propellant fed through the tube, the ions are constrained near the axis by the radially inward Lorentz force. On-axis ohmic heating in the MPD and FPPT are similar, and both thrusters operate in a similar range of specific impulse and generate similar electrothermal thrust fractions.

In region II, where the bulk of the thrust is generated, the ion and electron Hall parameters play an important role, again in a fashion similar to an MPD thruster.

Detailed spectroscopic, time-resolved photographic and magnetic probing of the discharge region remains to be accomplished to verify the unsteady time behavior and the degree of azimuthal symmetry in the discharge. Asymmetry may lead to an off-axis thrust component. Severe asymmetry could lead to spoking, with the discharge located at a single azimuthal location, but no evidence of this has been observed with the FPPT. Probing will also determine if the discharge is in a deflagration mode, as is now suspected.

X. Acknowledgments

This work was supported by NASA's SBIR program on contract numbers NNX17CP36P and 80NSSC18C0063. The authors thank Richard Hofer of the NASA Jet Propulsion Laboratory for his guidance and support. We also thank Jared Bowman and Magda Parta for assistance with FPPT data acquisition.

XI. References

- Antonsen, E. L., Burton, R. L., Reed, G. A., Spanjers, G. G., "Effects of Post Pulse Surface Temperature on MicroPPT Operation," *Journal of Propulsion and Power*, Vol. 21, No. 5, 877-883, Sept-Oct 2005.
- Benson, S. W., Arrington, L. A., Hoskins, W. A. and Meckel, N. J., "Development of a PPT for the EO-1 Spacecraft," NASA TM-2000-210340, AIAA Paper # 99-2276, 2000.
- Benson, S. W., and Frus, J.R. "Advanced Pulsed Plasma Thruster Electrical Components," AIAA 36th Joint Propulsion Conference, Salt Lake City, UT, AIAA Paper # 2001-3894, July 2001.
- Burkhardt, L. C., and Lovberg, R. H., "Current Sheet in a Coaxial Plasma Gun," *Phys. Fluids*, Vol. 5, 341-347, 1962.
- Burton, R. L., "Conditions for the Steady One-Dimensional Motion of a Current Sheet," *Phys. Fluids*, **11**, 2284, 1968.
- Burton, R. L., Devillers, P., and Chang, O., "Effect of Mass Injection on a High-Current Arc," *AIAA Journal*, Vol. 8, 1111-1116, 1970.
- Burton, R. L., K.E. Clark, K. E., and Jahn, R. G., "Measured performance of a multimewatt MPD thruster," *Journal of Spacecraft and Rockets*, Vol. 20, No. 3, 299-304, 1983.
- Burton, R. L. and Turchi, P. J., "Pulsed Plasma Thruster," *J. Propulsion and Power*, Vol. 14, No. 5, 716, 1998.

- Burton, R. L., Rysanek, F., Antonsen, E. A., Wilson, M. J., and Bushman, S. S., "Pulsed Plasma Thruster Performance for Microspacecraft Propulsion," AIAA Progress Series, Vol. 187, Micropropulsion for Small Spacecraft, M. Micci, ed., Chapter 13, 337 – 352, 2000.
- Burton, R. L., Benavides, G., and Laystrom, J., "Advanced Pulsed Plasma Thruster with High Electromagnetic Thrust," U.S. Patent No. 7,530,219 B1, May 12, 2009.
- Burton, R. L., Benavides, G., and Laystrom, J., "Advanced Pulsed Plasma Thruster with High Electromagnetic Thrust (Divisional 1)," U.S. Patent No. 7,926,257, April 19, 2011a.
- Burton, R. L., Benavides, G., and Laystrom, J., "Advanced Pulsed Plasma Thruster with High Electromagnetic Thrust (Divisional 2)," U.S. Patent No. 7,926,258, April 19, 2011b.
- Cheng, D. Y., "Application of a Deflagration Plasma Gun as a Space Propulsion Thruster," *AIAA Journal*, Vol. 9, No. 9, pp. 1681– 1685, 1971.
- Cohen, I. M. and Whitman, A. M., "On the Steenbeck minimum principle for arc discharges and its comparison with the constant property arc," *Journal of Applied Physics*, Vol. 44, 1557, 1973.
- Dali, H., Wansheng Z. and Xiaoming, K., "Operation analysis of pulsed plasma thruster," *Acta Astronautica*, Vol. 62, 404-409, 2008.
- Ekdahl, C., Kribel, R., and Lovberg, R., "Internal Measurements of Plasma Rotation in an MPD Arc," AIAA Paper # 67-655, 1967.
- Ebert, W. L., Kowal, S. J., and Sloan, R. F., "Operational Nova Spacecraft Teflon Pulsed Plasma Thruster System," AIAA Paper # 89-2497, 1989.
- Guman, W. J., "Switch-Triggered Pulse Plasma Accelerator Thrust Measurements," AIAA J., **3** (6), 1158, 1965.
- Guman W. J. and Nathanson, D. M., "Pulsed Plasma Micro-thruster Propulsion System for Synchronous Orbit Satellite," *J. Spacecraft and Rockets*, **7** (4), 409-15, 1970.
- Hoffman, E. J., "Spacecraft Design Innovations in the APL Space Department," Johns Hopkins APL Technical Digest, Vol. 13, No. 1, 167-181, 1992.
- Huang, T., et al., "Study of breakdown in an ablative pulsed plasma thruster," *Physics of Plasmas*, **22**, 103511, 2015.
- Jahn, R. G., "Physics of Electric Propulsion." McGraw-Hill, New York, 1968.
- Krejci, D., Seifert, B, and Scharlemann, C., "Endurance testing of a pulsed plasma thruster for nanosatellites," *Acta Astronautica*, Vol. 91, 187–193, 2013.
- Laystrom, J., Burton, R., and Benavides, G., "Geometric Optimization of a Coaxial Pulsed Plasma Thruster", AIAA Paper # 2003-5025, 2003.
- Megli, T.W., Krier, H., and Burton, R.L., "Plasmadynamics Model for Nonequilibrium Processes in N₂/H₂ Arcjets," *J. Thermodynamics & Heat Transfer*, **10** (4), 554, 1996.
- Palumbo, D. J., Begun, M., and Guman, W. J., "Electrode Erosion Processes in Pulsed Plasma Thrusters," Final Report AFRPL-TR-79-14, 1979.
- Polzin, K., "Pulsed Plasma Acceleration Modeling in Detonation and Deflagration Modes," IEPC 2019-893, 2019.
- Schwirzke, F., Hallal, M. P., AND Maruyama, X. K., "Onset of Breakdown and Formation of Cathode Spots," *IEEE Transactions on Plasma Science*, Vol. 21, No. 5, 410-415, 1993.
- Vondra, R. J., and Thomassen, K. I., "Flight Qualified Pulsed Electric Thruster for Satellite Control," *Journal of Spacecraft and Rockets*, Vol. 11, No. 9, 613-617, 1974.
- Vondra, R. J., "Pulsed Plasma Propulsion System/Spacecraft Design Guide," Final Report, AFRPL-TR-80-38, Air Force Rocket Propulsion Laboratory, TRW Defense and Space Systems Group, 1980.
- Wang, W., Kong, L, Geng, J., Wei, F., and Xia, G., "Wall ablation of heated compound-materials into non-equilibrium discharge plasmas," *J. Phys. D: Appl. Phys.*, **50**, 074005, 2017.
- Woodruff, C., King, D., Burton, R., Bowman, J., and Carroll, D., "Development of a Fiber-Fed Pulsed Plasma Thruster for Small Satellites," Small Satellite Conference, Paper # SSC19-WKVIII-06, 2019a.
- Woodruff, C., King, D., Burton, R., and Carroll, D., "Fiber-Fed Advanced Pulsed Plasma Thruster (FPPT)", U.S. Patent Applications # 16/436,149, 2019b.
- Woodruff, C., King, D., Burton, R., and Carroll, D., "Fiber-Fed Advanced Pulsed Plasma Thruster (FPPT) – Continuation-in-Part", U.S. Patent Applications # 16/439,755, 2019c.
- Zakrzewski, C., Benson, S., Sanneman, P., and Hoskins, A., "On-Orbit Testing of the EO-1 Pulsed Plasma Thruster," AIAA Paper # 2002-3973, 2002.